IRAQI BULLETIN OF GEOLOGY AND MINING (IBGM)
IRAQ GEOLOGICAL SURVEY (GEOSURV-IRAQ)

Vol.20, No.2, 2024 ***p 93 – 109***

RELOCATION AND STRESS ANALYSIS OF THE 2018 MANDALI-SUMAR EARTHQUAKE SEQUENCE, IRAQ – IRAN BORDER

Muntadher Al-Kaabi[1*], Dania Hantoosh[1], Wathiq Abdulnaby[1]

[1] Seismological Laboratory of University of Basrah (SLUB), Department of Geology, College of Science, University of Basrah, Basrah, Iraq, *Correspondence e-mail: malkaabi@ualr.edu

Type of the Paper: Article
Received: 21/ 08/ 2023
Accepted: 25/ 10/ 2023
Available online: November 06, 2024

Keywords: Relocation earthquakes; Zagros Fold-Thrust Belt; Stress analysis; Seismicity of Iraq; Moment tensor solutions.

ABSTRACT

The 2018 Mandali-Sumar earthquake sequence started in January 2018 at the Iraq – Iran border within the Low Folded Zone of the Zagros Fold-Thrust Belt. To study the fault that is responsible for this earthquake sequence, the relocation of 32 earthquakes was conducted. In addition, moment tensor solutions of 9 large earthquakes were collected to know the fault motion and stress regime in the study area. The Computer Programs in Seismology (CPS) was used to analyze waveform data taken from 33 seismic stations located in Iraq and Iran to relocate earthquakes. The location of the earthquake sequence based on the IRSC bulletin shows a scattered spatial distribution, but the results of the relocations show that the earthquakes of the sequences are aligned in a longitudinal feature parallel to an anticline limb located in Ilam and Kermanshah provinces near the Iraqi border. The moment tensor solutions indicate that the sequence is related to a thrust fault with a 342º strike direction, 35º NE dip angle, and 76º rake angle. The TENSOR program was used to perform formal stress inversion of moment stress axes, which revealed that the azimuth of the maximum horizontal stress axis is 63º. The epicenters of the sequence are located between the Mountain Front Fault to the NE and the Zagros Foredeep Fault to the Southeast. We believe that the 2018 Mandali-Sumar earthquake sequence is related to displacement on the surface of the Zagros Foredeep Fault within the uppermost basement and the lowermost Phanerozoic cover.

1. INTRODUCTION

Based on the tectonic divisions of Iraq, the study area is located within the Low Folded Zone of the Zagros Fold-Thrust Belt (Jassim & Goff, 2006; N. M. S. Numan, 1997); and (S. F. A. Fouad, 2015). Similarly, based on the tectonic division of Iran, the study area is located within the Simply Folded Belt (Casciello et al., 2009); (Karasözen et al., 2019) (Figure 1). The Zagros Fold-Thrust Belt is characterized by deformed crustal rocks that originated from the collision between the Arabian and Eurasian plates. The zone continues to exhibit tectonic activity, which is evident from the presence of folding and faulting (Tchalenko & Braud, 1974). Therefore, the Zagros Fold-Thrust Belt is one of the most seismically active mountain ranges.

The Low Folded Zone (Simply Folded Belt) is characterized by long anticlines with Neogene cores and broad synclines containing thick Miocene-Quaternary molasses (Jassim & Goff, 2006). Shortening in the Low Folded Zone varies from 3% to 17% based on fieldwork

ISSN 1311–4539
https://doi.org/10.59150/ibgm2001a06
IBGM: http://ibgm-iq.org/
Academic Scientific Journals: www.iasj.net

studies conducted by (Ameen, 1991a, 1991b, 1992). Mesozoic and Tertiary successions are mostly well-exposed in the zone within the anticlinal and synclinal structures, whereas Paleozoic successions are covered (S. F. A. Fouad, 2012).

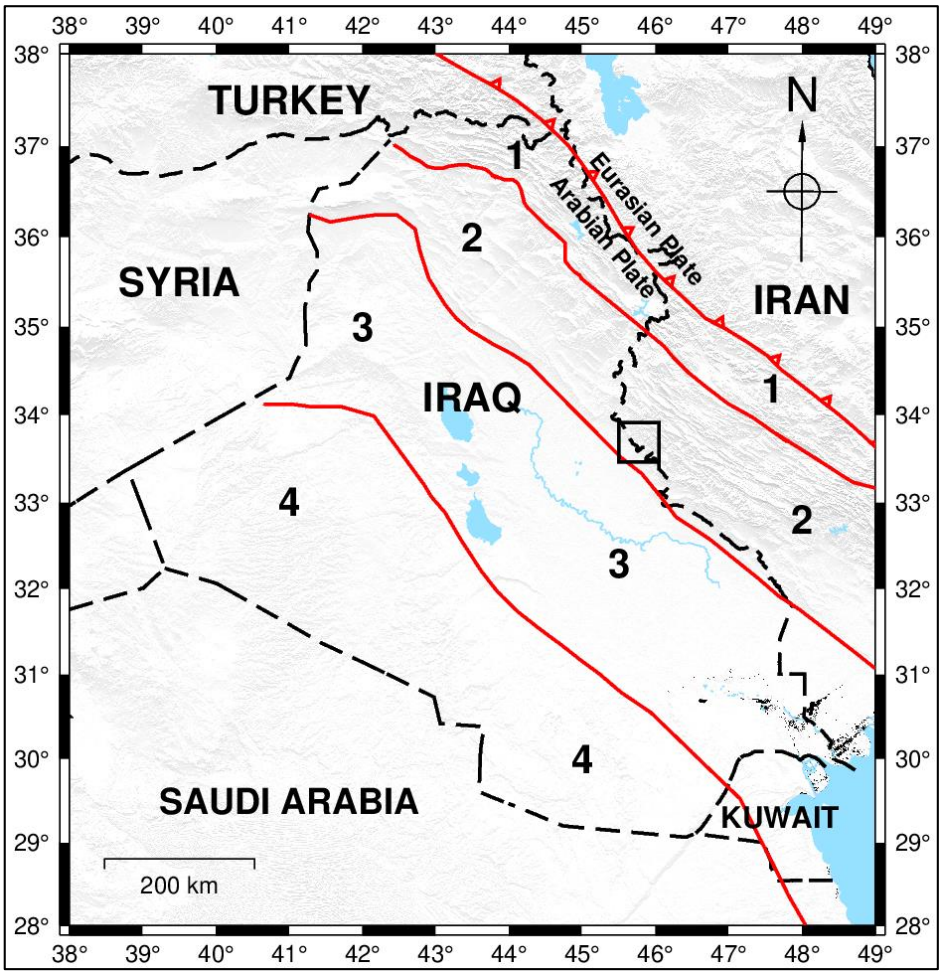

Figure 1: Location map of the study area with the tectonic division (red lines) according to (S. F. A. Fouad, 2015; Karasözen et al., 2019; Sissakian et al., 2017). The black square represents the study area. The black dashed line is the border of countries. **1**) Zagros Thrust (Thrust, Imbricated, and High Folded Zones). **2**) Simply Folded Belt (Low Folded Zone). **3**) Mesopotamia Foredeep. **4**) Inner Arabian Platform.

In the Low Folded Zone, anticlines are generally asymmetric and can be classified into two main types, simple buckle folds and fault-related folds (N. Numan & Azzawi, 1993). The fault-related folds are associated to basement reactivation, which resulted in reverse displacements on previously normal listric faults as well as strike-slip faults or wrench tectonics between basement blocks (N. M. S. Numan, 1984, 2000). The listric fault strikes are parallel to the anticline axes (N. Numan & Azzawi, 1993).

The Low Folded Zone is a seismically active region where many earthquakes with magnitudes ≤ 6 and focal depths ≤ 20 Km occur annually (Nissen et al., 2011). However, the largest recorded earthquake in the Simply Folded Belt occurred near the Iranian town of Ezgeleh-Sarpolzahab on 12 November 2017 with 7.3 Mw. Two months later, a sequence of five earthquakes ranging from 5.0 to 5.6 Mw occurred on January 11, 2018, followed by more than 200 aftershocks. This study specifically focuses on the 2018 sequence, known as the "Mandali-

Sumar earthquake sequence," which took place on the Iraq – Iran border between the cities of Mandali and Sumar.

(Barnhart et al., 2018) and (Nissen et al., 2019) studied the Mandali-Sumar 2018 earthquake sequence by mainly using the interferometric synthetic aperture radar (InSAR). (Barnhart et al., 2018) found that the moderate magnitude earthquakes of this sequence were caused by a reverse fault with NE dipping that ruptured the lower Phanerozoic cover of the Zagros.

(Nissen et al., 2019) proposed that the 2018 Mandali-Sumar earthquake sequence can be reproduced with buried reverse slip on either a NE or SW dipping fault, but they prefer the former geometry because it produces slightly smaller residuals and closely resembles the location and orientation of the NE dipping Zagros Foredeep Fault. Additionally, they found that the center depth of the InSAR model fault plane is well resolved at about 11 Km, closely matching the centroid depth for the Mw 5.5 06:59 main shock determined by teleseismic body wave modeling of about 12 Km. Since the cover thickness in the study area has been estimated to range from about 10 to 13 Km, they suggested that the Mandali-Sumar earthquakes may have ruptured the lowermost cover, the uppermost basement, or both.

The objective of this research is to investigate the fault responsible for the 2018 Mandali-Sumar earthquake sequence through a comprehensive approach. This involves utilizing the earthquake catalog of the Iranian Seismological Center (IRSC) and relocating earthquakes by analyzing seismic waveform data recorded in seismic stations in Iraq and Iran. Moment tensor solutions from various sources for earthquakes of the sequence will also be collected to study the fault motion, followed by conducting the stress analysis through formal stress inversion of moment stress axes. Moreover, the spatial distribution of hypocenters and epicenters will be analyzed and compared with the structural and tectonic setting of the study area to construct a simple structural cross-section that explains the reason behind the seismic activity in the area.

2. THE 2018 MANDALI-SUMAR EARTHQUAKE SEQUENCE

The study area is seismically active based on the bulletin of the Iranian Seismological Center (IRSC). Since 2006, three earthquake sequences occurred in 2014, 2018, and 2019. The largest sequence is the one that occurred in 2018. This earthquake sequence commenced on January 11th, 2018, and persisted until November 7th, 2018. Figure 2 is a histogram showing the number of earthquakes for each month. The total number of earthquakes in this sequence based on the IRSC bulletin is 384. Most of them (288) occurred in January, which represents 75% of the whole earthquake sequence (Figure 2).

The main shock of the sequence has a magnitude of 5.6 Mw. During the 22 minutes after the main shock, three earthquakes with magnitudes of 5.1, 5.4, and 5.2 Mw struck the area. Then it was followed by earthquakes with lower magnitudes that reached a magnitude of 2.5 MN, which is the lowest recorded magnitude. Figure 3 represents the magnitude-frequency distribution of the 2018 earthquake sequence.

The spatial distribution of the 2018 Mandali-Sumar earthquake sequence is represented in Figure 4. The figure shows scattered spatial distribution, which indicates low accuracy of epicentral locations. Therefore, 32 earthquake data were selected for relocation. The selection of these events was based on two primary factors: data availability and the quality of recorded events. We focused on earthquakes for which data were readily available and those that were recorded clearly without significant noise in our station. A list of the selected earthquakes is shown in Table 1. It is worth mentioning that the majority of the earthquake epicenters of this sequence are located between the Mountain Front Fault (MFF) and the Zagros Foredeep Fault

(ZFF). These two faults are discontinuous lines and are roughly parallel to each other, exhibiting a reverse displacement and seismically active behavior (Al-Kaabi & Abdulnaby, 2022; Berberian, 1995).

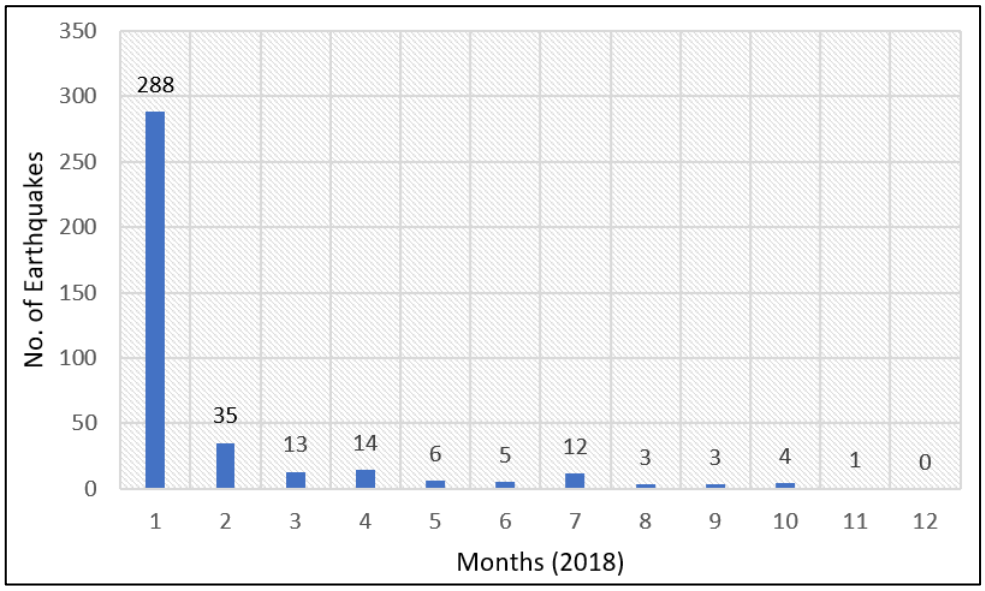

Figure 2: Temporal distribution of the 2018 earthquake sequence according to the IRSC bulletin.

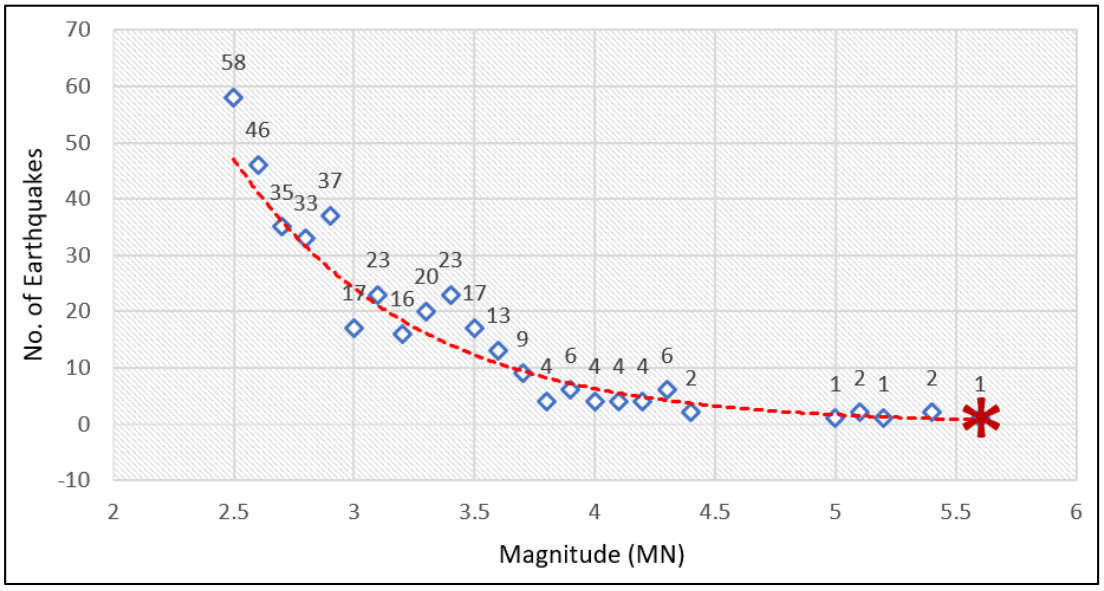

Figure 3: Magnitude-frequency distribution of earthquakes larger than magnitude 2.5 in the 2018 earthquake sequence taken from the IRSC bulletin. The red star represents the main shock, the reversed squares represent the aftershocks, and the dashed line represents the trend of increasing earthquake numbers with decreasing magnitude.

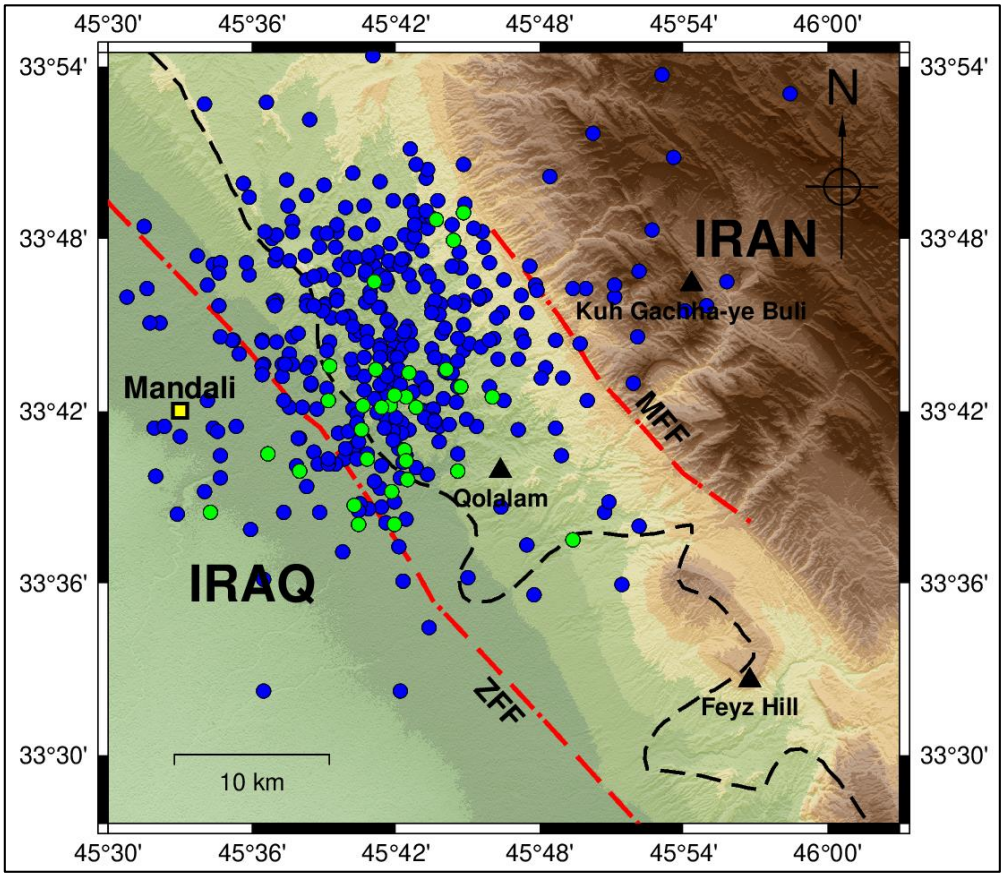

Figure 4: Spatial distribution of the Mandali-Sumar earthquake sequence based on the Iranian Seismological Center (IRSC). The green circles represent earthquakes selected for relocation as shown in Table 1. The black triangles are the summits of mountains in the study area. MFF is the Mountain Front Fault and ZFF is the Zagros Foredeep Fault.

Table 1: Basic source parameters of selected earthquakes of the 2018 earthquake sequence taken from the Iranian Seismological Center (IRSC). RMS error is the location root mean Square Error.

No.	Date (Y/MM/DD)	Time (UTC)	Lat. (°)	Long. (°)	Depth (km)	Mag. (MN)	RMS error	Gap (°)
1	2018/01/11	06:59:29.8	33.712	45.693	8.4	5.6	0.5	219
2	2018/01/11	07:14:15.5	33.722	45.709	9.4	5.4	0.4	215
3	2018/01/11	07:52:47.9	33.815	45.747	11.8	4.3	0.4	211
4	2018/01/11	08:00:39.1	33.724	45.686	10.9	5.4	0.7	215
5	2018/01/11	08:25:35.0	33.665	45.633	9.3	3.7	0.3	241
6	2018/01/11	08:53:34.1	33.703	45.677	9.3	3.9	0.2	218
7	2018/01/11	09:23:55.7	33.677	45.706	13.4	4.1	0.4	216
8	2018/01/11	09:32:24.9	33.706	45.653	8.0	4.2	0.4	216
9	2018/01/11	10:14:10.1	33.703	45.696	8.0	3.6	0.2	254
10	2018/01/11	10:41:27.9	33.672	45.680	13.0	3.6	0.3	219
11	2018/01/11	13:16:43.0	33.724	45.735	7.7	4.3	0.3	214
12	2018/01/11	20:19:40.2	33.653	45.697	8.0	4.0	0.4	216
13	2018/01/11	21:50:44.2	33.775	45.685	8.0	4.4	0.3	215
14	2018/01/12	07:49:26.7	33.714	45.745	8.2	3.4	0.1	234
15	2018/01/12	11:43:48.7	33.702	45.690	8.8	3.9	0.2	217
16	2018/01/12	17:50:40.5	33.645	45.671	7.3	4.3	0.3	216

Continue Table 1:

No.	Date (Y/MM/DD)	Time (UTC)	Lat. (°)	Long. (°)	Depth (km)	Mag. (MN)	RMS error	Gap (°)
17	2018/01/13	00:33:26.8	33.660	45.708	8.0	4.2	0.5	216
18	2018/01/13	06:30:30.3	33.671	45.707	8.0	4.3	0.3	236
19	2018/01/13	09:31:53.8	33.726	45.654	7.7	4.1	0.3	219
20	2018/01/14	17:17:05.7	33.665	45.743	9.1	3.5	0.3	245
21	2018/01/15	15:04:58.0	33.689	45.676	11.2	3.5	0.4	239
22	2018/01/16	19:56:25.5	33.811	45.728	8.0	3.6	0.2	236
23	2018/01/18	02:54:49.0	33.708	45.767	8.5	3.6	0.4	213
24	2018/01/19	22:17:56.0	33.709	45.699	8.8	5.0	0.6	215
25	2018/01/26	20:17:34.4	33.675	45.611	8.0	4.4	0.4	192
26	2018/01/28	04:07:09.0	33.799	45.740	12.2	3.6	0.2	232
27	2018/01/31	17:53:24.8	33.702	45.714	12.2	3.5	0.2	236
28	2018/02/06	12:28:25.3	33.625	45.823	11.2	3.6	0.6	231
29	2018/02/10	17:41:22.6	33.708	45.707	8.0	3.6	0.5	216
30	2018/02/16	18:22:00.1	33.634	45.699	12.2	4.0	0.3	216
31	2018/04/21	14:18:11.3	33.641	45.571	9.4	3.5	0.5	242
32	2018/08/11	19:10:48.4	33.634	45.674	9.0	3.7	0.3	239

3. METHODS, DATA, AND SOFTWARE

3.1. Earthquake Location

The earthquake hypocenter (focus) is determined by latitude, longitude, and depth, but only latitude and longitude are used to determine the epicenter, which is where the focus is projected to the surface (Havskov & Ottemoller, 2010). The location of local earthquakes with an epicentral distance of less than 10º was conducted in this study. The earthquake location is determined by selecting the seismic wave arrival times. It is the first and most crucial task in earthquake analysis. The P and S phases were picked. Different filters can be applied to digital recordings to highlight specific waves and reduce noise, but this can cause additional phase shift problems. At least, three seismic stations were used to locate earthquakes. However, it is possible to locate occurrences with fewer than three stations. In this study, the iterative method is used to determine the location. (Geiger, 1910) used this technique for the first time, which is why it is known as the Geiger method. For more details on the Geiger method, see (Havskov & Ottemoller, 2010).

Seismic velocity models are critical for earthquake location. It is a basic set of data used to calculate the epicentral distance based on travel time. The velocity model is region-specific and is calculated using earthquake data accumulated in that region. In this study, the Western United States (WUS) velocity model was applied to relocate the selected earthquake because this model is representative of the geology of the Bitlis-Zagros Fold-Thrust Belt due to the geological similarity.

In this study, data from 8 seismic stations of the Mesopotamian Seismological Network (MPSN), 13 seismic stations of the Iranian Seismological Center (IRSC), and 12 seismic stations of the Iranian National Seismological Network (INSN) were used to relocate 32 selected earthquakes. Table 2 shows the station names, codes, locations, elevations, and types of seismic stations. Figure 5 depicts the geographical distribution of these stations regarding the study area. Figure 6 represents an example of waveform data used in relocating the earthquake that occurred on January 26, 2018 (see the earthquake of 2018/01/26-20:17:35 in Table 1).

The Computer Program in Seismology (CPS) version 3.30 by (Herrmann, 2013) was used to relocate earthquakes in this study. The CPS is a package that contains more than 150 programs that can be run by scripts. These programs allow us to understand and interpret the seismic wave propagation in the crust and mantle of the earth. Specifically, the GSAC, SAC2ELOC, and ELOCATE programs were utilized to relocate earthquakes in this study, yielding essential parameters such as the original time, date, latitude, longitude, and depth.

Table 2: Seismic stations used in this study. All stations are broadband except HALM and RAZ, which are short-period.

Network	Station Name	Station Code	Latitude (°)	Longitude (°)	(m) Altitude
MPSN	Amarah	AMR2	31.9899	47.1902	10
	Anbar	ANB1	33.4013	43.2576	52
	Basrah	BSR2	30.2927	47.6191	16
	Duhok	DHK1	36.8606	42.8665	766
	Karbala	KAR2	32.5398	44.0224	45
	Kirkuk	KIR1	35.3880	44.3419	290
	Nasiriyah	NSR4	31.5399	46.2016	7
	Sulaymaniyah	SLY1	35.5784	45.3667	756
IRSC	Ahwaz	AHWZ	31.330	48.644	19
	Almabolaq	HALM *	34.860	48.168	2450
	Aqdareh	HAGD	34.822	49.139	1831
	Bozab	BZA	34.470	47.861	2330
	Dareh Seyedi	BDRS	33.954	48.881	2494
	Doab	DOB	33.787	48.177	1948
	Kafar Mosalman	KFM	33.524	47.847	1676
	Mahabad	MAHB	36.767	45.705	1370
	Masjed Soleyman	AMIS	31.665	49.287	442
	Razeqan	RAZ *	35.405	49.929	1950
	Samen	HSAM	34.212	48.602	2314
	Sardasht	SDS1	36.149	45.486	1591
	Sonqor	SNQR	34.858	47.628	2502
INSN	Ashtian	ASAO	34.548	50.025	2217
	Charan (Alborz)	CHTH	35.908	51.126	2350
	Damavand	DAMV	35.630	51.971	2520
	Ghom	GHVR	34.480	51.295	927
	Hashtgerd	THKV	35.916	50.879	1795
	Ilam	ILBA	33.560	46.210	799
	Khomeyn	KHMZ	33.739	49.959	1985
	Ramhormoz	RMKL	30.982	49.809	176
	Sanandaj	SNGE	35.093	47.347	1940
	Sardasht	SRSL	36.210	45.430	1745
	Shushtar	SHGR	32.108	48.801	150
	Zanjan	ZNJK	36.670	48.685	2200

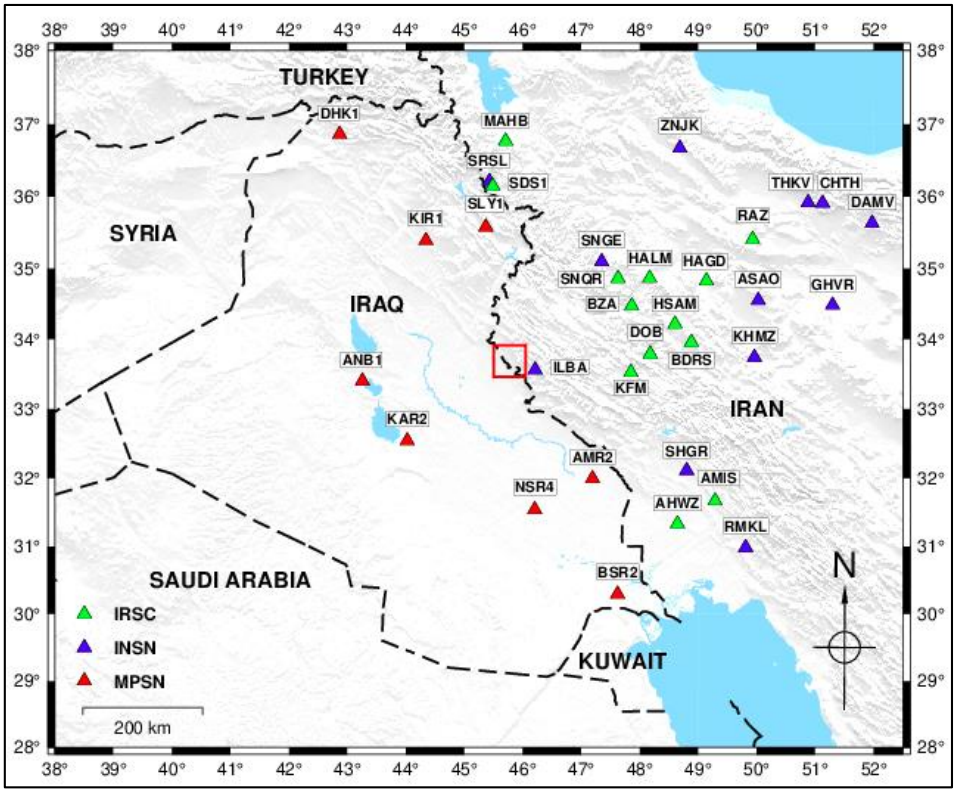

Figure 5: Location map of local seismic stations (epicentral distance < 10º) used in this study, which belongs to three seismological networks, these are MPSN, IRSC, and INSN. The study area is represented by the red square.

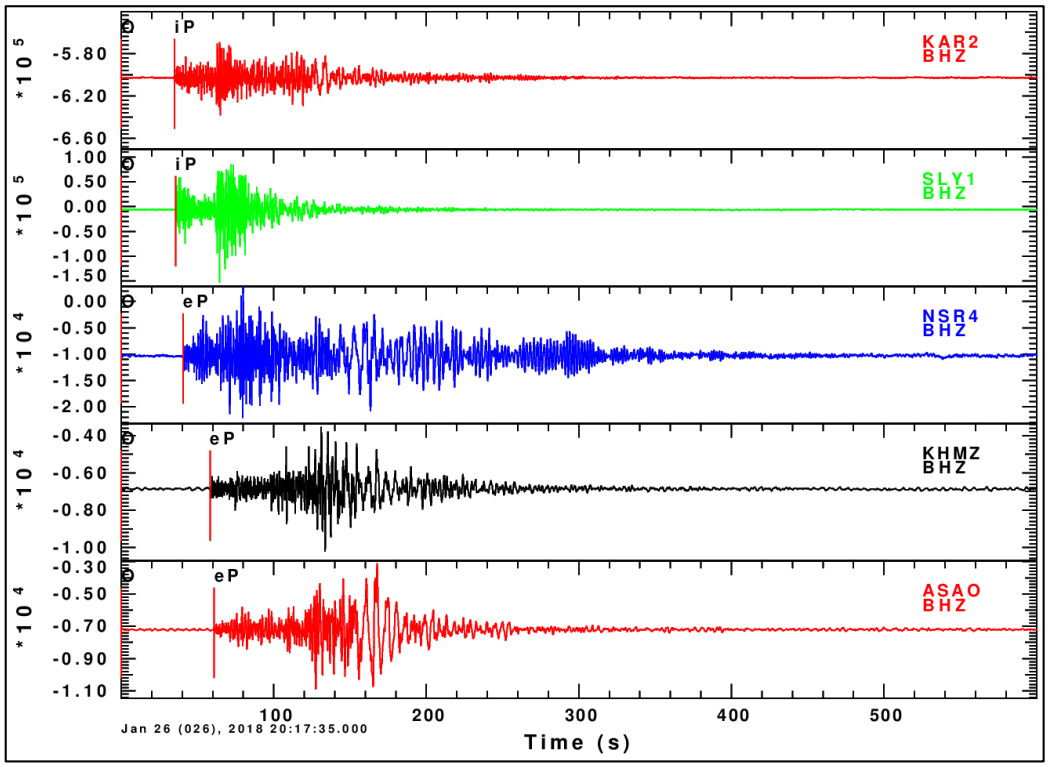

Figure 6: An example of seismic waveforms used in the relocation of an earthquake that occurred on January 26, 2018 (see the earthquake of 2018/01/26-20:17:35 in Table 1).

3.2. Focal Mechanism Solutions

The focal mechanism solution, also known as the fault plane solution, describes the fault geometry, the style of faulting, and the stress regimes. The focal mechanism solution can be determined once the location and magnitude of an earthquake are known. All seismological methods for determining focal mechanism solutions rely on the radiation pattern produced by the seismic earthquake source (Havskov & Ottemoller, 2010).

The current study retrieved the focal mechanism solutions of nine earthquakes from various sources, including the Global Centroid Moment Tensor (GCMT), the Iranian Seismological Center (IRSC), and (Mohammed & Al-Rahim, 2020). These sources employed the moment tensor inversion method to estimate the focal depths, moment magnitudes, fault plane solutions, and moment stress axes.

The formal stress inversion of moment stress axes (P, N, and T) gives the four parameters of the reduced stress tensor; these are the three principal stress axes (σ1, σ2, and σ3) and the stress ratio $R = (\sigma2 - \sigma3)/(\sigma1 - \sigma3)$. In this study, two methods of stress inversion are used; these are the improved right dihedron and the rotational optimization methods. (Lund & Townend, 2007) developed a mathematical method to compute the true direction of the maximum (SH) and minimum (Sh) horizontal stress axes from the four stress tensor components (σ1, σ2, σ3, and R). All of these methods are implemented in a free source program named TENSOR which was developed originally in a DOS operating system by (Delvaux, 1993). Then it was developed in Windows by (Delvaux & Sperner, 2003). In this study, the Windows Win-Tensor version 5.9.2 was used to invert the moment stress axes to the principal stress axes, the stress ratio, and the horizontal stress axes. See (Abdulnaby et al., 2014) for more information on the methods and the TENSOR program.

4. RESULTS AND DISCUSSION

4.1. Relocation

As mentioned earlier, an earthquake sequence occurred in the study area started in January 2018. To study the sequence, 32 earthquakes were selected to be relocated using data from the MPSN, IRSC, and INSN seismic networks. The results of relocating the selected earthquakes are shown in Table 3.

The azimuthal gap is the largest angle between the azimuths of two adjacent seismic stations that are measured from the epicenter of an earthquake and the station. The location accuracy degrades significantly if the azimuthal gap is more than 180°, which indicates that all the stations are located on one side of the event (Havskov & Ottemoller, 2010; Tiira et al., 2016). A comparison of Tables 1 and 3 reveals that the azimuthal gap reported by the IRSC is greater than 180 (ranging from 211 to 264), whereas the present study reports an azimuthal gap of less than 180 (ranging from 84 to 175). These findings suggest that the location accuracy achieved in this study is superior to that reported by the IRSC.

The root mean squared (RMS) is a commonly used parameter to assess the location accuracy of earthquakes. It is calculated based on the difference between observed and predicted arrival times of seismic waves and indicates the quality of the data fit. However, the precision of the velocity model used to calculate the earthquake location, the assigned weights to the arrival time data, and the method employed to locate the earthquake can affect the RMS value. It should be noted that RMS only measures the fit of the data and does not necessarily reflect a precise hypocenter determination (Havskov & Ottemoller, 2010). Comparing the RMS values in Tables 1 and 3 demonstrates that the fit of our data is higher than that of the IRSC

data, as the RMS values range from 0.02 to 0.4 for our data and from 0.2 to 0.7 for the IRSC data.

Table 3: Relocated events of the 2018 Mandali-Sumar Sequence selected events. RMS error is the location root mean Square Error. Error ellipse is the location uncertainty in both east-west (X) and north-south (Y).

No.	Date (Y/MM/DD)	Time (UTC)	Lat. (°)	Long. (°)	Depth (Km)	Mag. (IRSC) (MN)	RMS error	Error ellipse			Gap (°)
								X-axis (Km)	Y-axis (Km)	Theta (°)	
1	2018/01/11	06:59:30.100	33.7323	45.7463	8.50	5.6	0.142	1.5239	1.8942	117.2642	116
2	2018/01/11	07:14:16.198	33.7216	45.7215	11.29	5.4	0.310	1.4946	2.3784	48.7742	120
3	2018/01/11	07:52:48.531	33.7666	45.7639	13.91	4.3	0.157	1.4651	2.0659	161.9277	119
4	2018/01/11	08:00:40.153	33.7070	45.7372	8.08	5.4	0.228	1.2210	1.8175	47.2021	121
5	2018/01/11	08:25:37.798	33.7845	45.7337	10.47	3.7	0.321	2.2297	3.6735	55.4749	150
6	2018/01/11	08:53:36.742	33.7664	45.7473	14.96	3.9	0.172	1.7049	2.3166	53.6883	151
7	2018/01/11	09:23:56.919	33.7121	45.8367	15.00	4.1	0.065	0.8781	1.8366	172.3088	148
8	2018/01/11	09:32:27.426	33.7767	45.7574	13.12	4.2	0.358	2.5026	2.6946	108.9377	119
9	2018/01/11	10:14:11.037	33.7454	45.7578	11.49	3.6	0.450	2.8506	3.5067	45.8973	119
10	2018/01/11	10:41:29.760	33.7455	45.7767	12.99	3.6	0.384	2.7102	3.1192	61.5424	118
11	2018/01/11	13:16:44.703	33.7447	45.7783	12.98	4.3	0.049	1.0288	1.0833	125.5229	134
12	2018/01/11	20:19:42.329	33.7286	45.7978	12.91	4.0	0.128	1.6784	1.7224	113.8969	135
13	2018/01/11	21:50:45.259	33.7665	45.7233	08.53	4.4	0.318	2.0274	2.3797	41.1989	121
14	2018/01/12	07:49:28.278	33.7200	45.8030	14.66	3.4	0.204	1.6550	2.5040	66.6139	136
15	2018/01/12	11:43:50.889	33.7466	45.7670	14.29	3.9	0.135	1.3970	1.4648	140.5459	118
16	2018/01/12	17:50:42.251	33.6824	45.7602	9.69	4.3	0.243	2.0871	3.1592	26.1573	124
17	2018/01/13	00:33:28.260	33.6571	45.7703	8.77	4.2	0.195	1.2022	1.5211	62.5228	128
18	2018/01/13	06:30:32.178	33.7122	45.7834	14.13	4.3	0.047	0.7447	1.0366	159.4335	117
19	2018/01/13	09:31:55.868	33.7923	45.7503	11.13	4.1	0.069	1.3102	7.1035	129.8572	151
20	2018/01/14	17:17:07.680	33.6845	45.8628	11.96	3.5	0.096	1.2127	1.4637	179.9877	113
21	2018/01/15	15:05:00.726	33.7155	45.8159	11.95	3.5	0.019	0.7978	0.8334	59.0158	136
22	2018/01/16	19:56:26.931	33.7963	45.7369	14.82	3.6	0.167	1.5619	1.7708	70.0691	131
23	2018/01/18	02:54:50.818	33.7193	45.8165	14.59	3.6	0.288	2.0629	2.5456	26.7182	116
24	2018/01/19	22:17:57.690	33.7526	45.6959	12.17	5.0	0.427	1.3395	1.8008	23.6931	121
25	2018/01/26	20:17:36.095	33.6372	45.9314	9.94	4.4	0.554	2.3837	3.7110	288.8857	110
26	2018/01/28	04:07:09.661	33.7646	45.7478	14.93	3.6	0.106	1.0625	1.3770	159.0219	119
27	2018/01/31	17:53:26.571	33.7027	45.8046	14.37	3.5	0.062	0.8643	1.0202	28.7295	116
28	2018/02/06	12:28:27.108	33.6560	45.8714	14.45	3.6	0.054	1.0200	1.3658	159.7801	175
29	2018/02/10	17:41:24.953	33.7606	45.7794	13.75	3.6	0.071	1.0269	1.1678	138.5827	118
30	2018/02/16	18:22:02.040	33.7081	45.8048	13.64	4.0	0.145	1.2701	1.6067	13.2179	116
31	2018/04/21	14:18:14.996	33.7572	45.7665	13.81	3.5	0.197	1.6768	1.8477	133.5355	119
32	2018/08/11	19:10:51.765	33.7288	45.8072	13.72	3.7	0.210	1.7287	2.3617	8.3346	93

The error ellipse only depends on the geometry of the network and the crustal structure. The error ellipses are larger for events outside the network than inside the network. The error in depth is also generally larger than the error in the epicenter as expected (Havskov & Ottemoller, 2010). Our results show that the range of error ellipse for the X-axis ranges from 0.7 to 2.8 Km and for the Y-axis from 0.8 to 3.7 Km (Table 3). We are unable to compare our error ellipse results with the IRSC since no error ellipse data is reported.

Plotting the epicenters of the relocated earthquakes on a map shows an aligned longitudinal feature located between Mandali and Sumar cities within the Iranian territories. Figure 7 represents the locations of these earthquakes before and after the relocation. The upper panel depicts the locations of the studied earthquakes taken from the IRSC that show a scattered distribution. The lower panel depicts the locations of the studied earthquakes based on the results of this study that show a longitudinal feature. The trend direction of this longitudinal feature is NW – SE, which is the trend of the Zagros Fold-Thrust Belt.

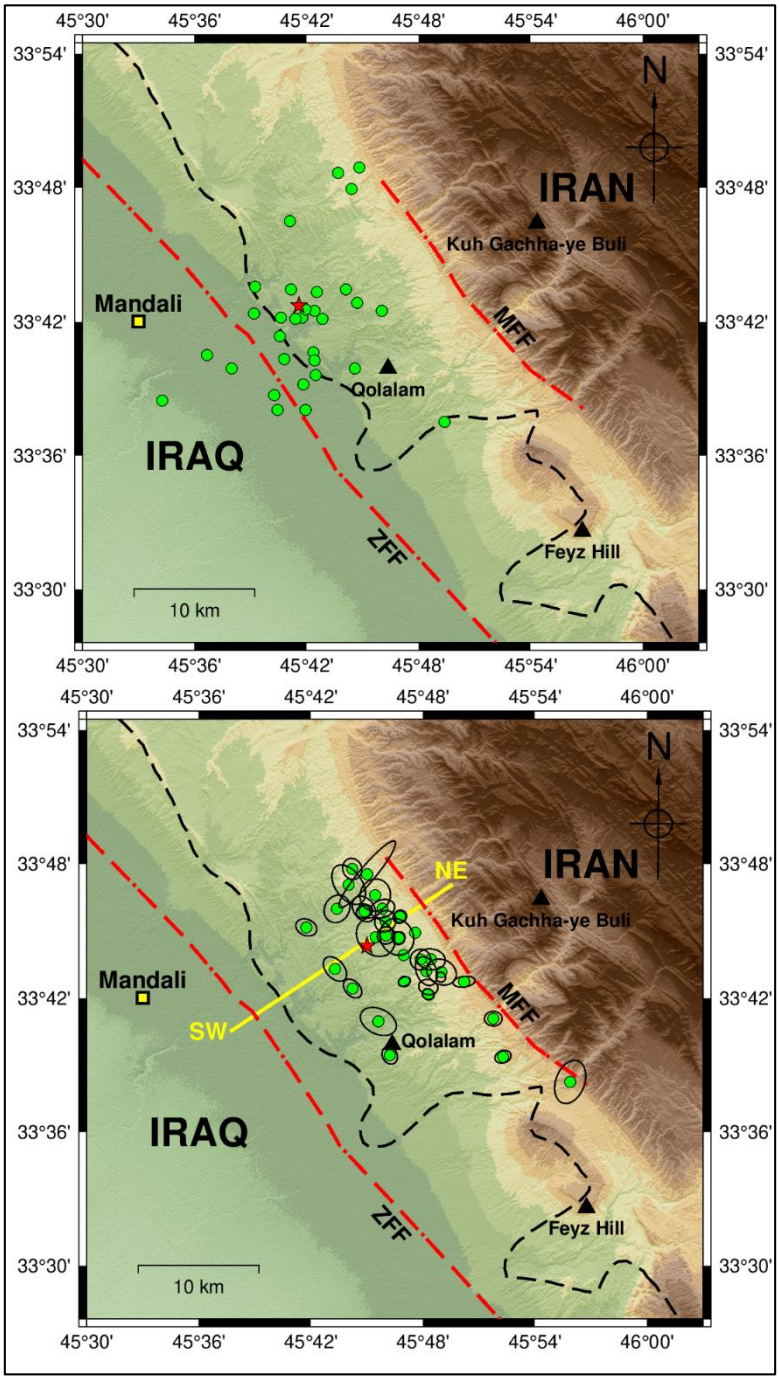

Figure 7: The selected earthquakes of the 2018 Mandali-Sumar earthquake sequence. The upper panel shows epicenters based on the IRSC bulletin. The lower panel shows the epicenters based on this study with their error ellipse (see Table 3). The red star is the epicenter of the main shock. The NE – SW line represents the direction of the cross-section in Figure 10.

It is pertinent to note that the relocated epicenters of the Mandali-Sumar earthquake sequence are located between the surface projections of the NE dipping Zagros Foredeep and Mountain Front Faults. The sedimentary Phanerozoic cover in the area between these two faults has been estimated to range from 10 to 13 km (Blanc et al., 2003; Emami et al., 2010; Farzipour Saein et al., 2009; McQuarrie, 2004).

4.2. Seismic Active Fault

The study area is part of the Low Folded Zone (Simply Folded Belt) that is characterized by longitudinal anticlines associated with faults (e.g. Abdulnaby, 2019; S. F. Fouad, 2012; N. Numan & Azzawi, 1993). The main structural feature in the study area is a longitudinal anticline with hinge line trends NW – SE, which is the Zagros trend. This anticline is called locally Kuh Gachha-ye Buli (in persian), which means the Mountain of Gypsum. A sharp change in elevation at the SW limb of the anticline can be seen clearly on the map plotted from the Digital Elevation Models (DEM) (Figure 7). This is because the SW limb of the anticline is limited to the trace of the Mountain Front Fault that dips toward NE. The seismic activity of the sequence is located at the SW of the fault. Thus, the fault cannot be responsible for the seismic activity of this sequence. The other fault that can be responsible for the seismic activity is the Zagros Foredeep Fault, which is located at the SW of the epicenters and dips toward NE (Figure 7).

4.3. Focal Mechanism Solutions

In order to investigate the slip motion on the Zagros Foredeep Fault, focal mechanism solutions from moment tensors of 9 earthquakes of the 2018 sequence were collected from different sources as shown in Table 4. The focal mechanism solutions revealed that all 9 earthquakes have oblique thrust motion mechanisms (Figure 8). The thrust mechanism is attributed to the compressional forces resulting from the collision between the Arabian and Iranian plates, while the oblique mechanism can be explained by the anticlockwise rotation of the Arabian plate. (Hancock & Atiya, 1979) suggested the anticlockwise rotation of the Arabian plate using fracture analyses. (N. M. S. Numan, 1984) concluded from the displacement of strike-slip faults in the basement a rotational movement of the basement rocks. Subsequently, (N. M. S. Numan, 2000) showed that the Alpine continental collision of the Arabian Plate started with the collision with the Turkish Plate and later proceeded to collide with the Iranian Plate. This collision implies an anticlockwise rotation of the Arabian plate.

Table 4: Source parameters of selected events in the study area (Table 3, International Seismological Center, International Data Centre, and Iranian Seismological Center) and focal mechanism solutions from the moment tensor inversion by (Mohammed & Al-Rahim, 2020), Iranian Seismological Center (IRSC), and Global Centroid Moment Tensor (GCMT). RD, relocated depth; MI, reported magnitude; CD, calculated depth measured in kilometers (km); Mw, moment magnitude; MO, seismic moment measured in dyne-cm; S, strike; D, depth measured in kilometers (km); R, rake angle; P, N, and T compressional, normal, and tensional moment stress axes, respectively, PL plunge angle, AZ azimuth.

No.	Date	Time (UTC)	Lat.	Long.	RD (km)	RM (ML)	CD (km)	Mw	Mo (dyne-cm)	Plane 1			Plane 2			Moment Stress Axes						Source
																P		N		T		
										S1 (°)	D1 (°)	R1 (°)	S2 (°)	D2 (°)	R2 (°)	PL (°)	AZ (°)	PL (°)	AZ (°)	PL (°)	AZ (°)	
1	2018/01/11	06:59:29.800	33.7388	45.7501	8	5.6	12	5.5	2.43e+17	146	45	082	337	46	098	00	062	-	-	84	327	IRSC
							20	5.6	3.51e+24	135	65	070	356	32	126	18	240	18	144	64	011	MOAL
							12	5.5	2.62e+24	142	43	072	346	50	106	03	065	12	155	77	319	GCMT
2	2018/01/11	07:14:19.000	33.7517	45.7428	9.40	5.4	14	5.3	1.02e+17	152	57	098	317	34	078	12	236	-	-	76	086	IRSC
							18	5.3	1.05e+24	160	65	090	340	25	090	20	250	00	340	70	070	MOAL
							16	5.4	1.65e+24	342	36	111	137	57	075	10	237	12	145	74	007	GCMT
3	2018/01/11	07:52:48.531	33.7666	45.7639	13.91	4.3	17	4.1	1.84e+22	177	57	130	300	50	045	04	240	33	333	57	144	MOAL
4	2018/01/11	07:55:04.600	33.7263	45.7837	8.20	5.1	13	4.8	2.32e+16	162	54	092	338	36	087	09	250	-	-	81	082	IRSC
							18	4.8	2.00e+23	150	80	070	034	22	153	32	257	20	154	51	037	MOAL
							12	5.0	4.25e+23	137	47	052	006	55	123	04	073	26	165	63	334	GCMT
5	2018/01/11	09:23:56.919	33.7767	45.7574	13.12	4.2	19	3.9	8.91e+21	130	65	065	358	35	132	16	238	23	141	62	001	MOAL
6	2018/01/11	13:16:44.703	33.7447	45.7783	12.98	4.3	18	4.2	2.60e+22	145	65	080	348	27	110	19	242	9	149	68	035	MOAL
7	2018/01/11	20:19:42.329	33.7286	45.7978	12.91	4.0	18	3.8	6.53e+21	168	62	101	325	30	070	16	250	10	342	71	102	MOAL
8	2018/01/13	06:30:32.178	33.7122	45.7834	14.13	4.3	17	3.8	6.53e+21	332	66	123	095	40	040	14	039	29	137	56	286	MOAL
9	2018/02/16	18:22:02.040	33.7081	45.8048	13.64	4.0	18	4.0	1.14e+22	155	89	096	255	05	010	44	240	05	335	46	070	MOAL

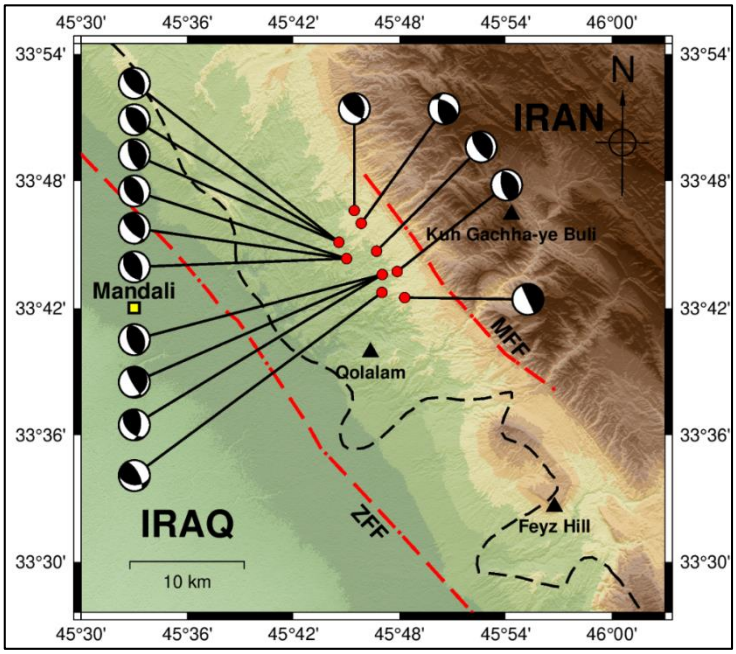

Figure 8: Focal mechanism solutions of 9 earthquakes of the 2018 Mandali-Sumar earthquake sequence. The focal mechanism solutions are taken from the GCMT, IRSC, and (Mohammed & Al-Rahim, 2020) as shown in Table 4.

Formal stress inversion of moment stress axes derived from the 9 focal mechanism solutions was conducted for the study area by applying the New Right Dihedron and the Rotational Optimization methods to get the principal stress axes and the horizontal stress axes. Figure 9 and Table 5 depict the results of applying formal stress inversion. These results are ambiguous because of having two plane solutions; these are the fault and the auxiliary planes. It is difficult to solve this ambiguity since the fault is buried and has no surface trace. However, the nodule plane with the NE dip direction is preferred because the study area is situated between the surface projections of the NE dipping Zagros Foredeep and Mountain Front Faults. Therefore, the fault plane solutions of the Zagros Foredeep Fault are 342º for the strike direction, 35º for the dip angle, and 76º for the rake angle. The directions of the maximum horizontal stress axis (SH) and the minimum horizontal stress axis (Sh) that are responsible for the fault movement are 63º and 153º, respectively.

The schematic representation in Figure 10 depicts a cross-section in the NE – SW direction through the proposed fault surface, exhibiting the hypocenter, epicenter, and focal depth of the main shock. The focal depths of the relocated earthquakes range from 8 to 15 Km (Table 3). The thickness of the sedimentary cover ranges from 10 to 13 km. Thus, we suggest that the displacement on the Zagros Foredeep Fault occurred within the uppermost basement and the lowermost sedimentary cover.

Table 5: Results of formal stress inversion of the rotational optimization method.

Selected Data	Fault Plane			Auxiliary Plane			Reduced stress tensor parameters							Horizontal stress axes		Stress regime	Quality
							σ_1		σ_2		σ_3		R				
	Strike	Dip	Rake	Strike	Dip	Rake	PL	AZ	PL	AZ	PL	AZ		SH	Sh		
20	342º	35º	76º	145º	56º	80º	11º	242º	08º	151º	77º	025º	2.5	63º	153º	TF	A

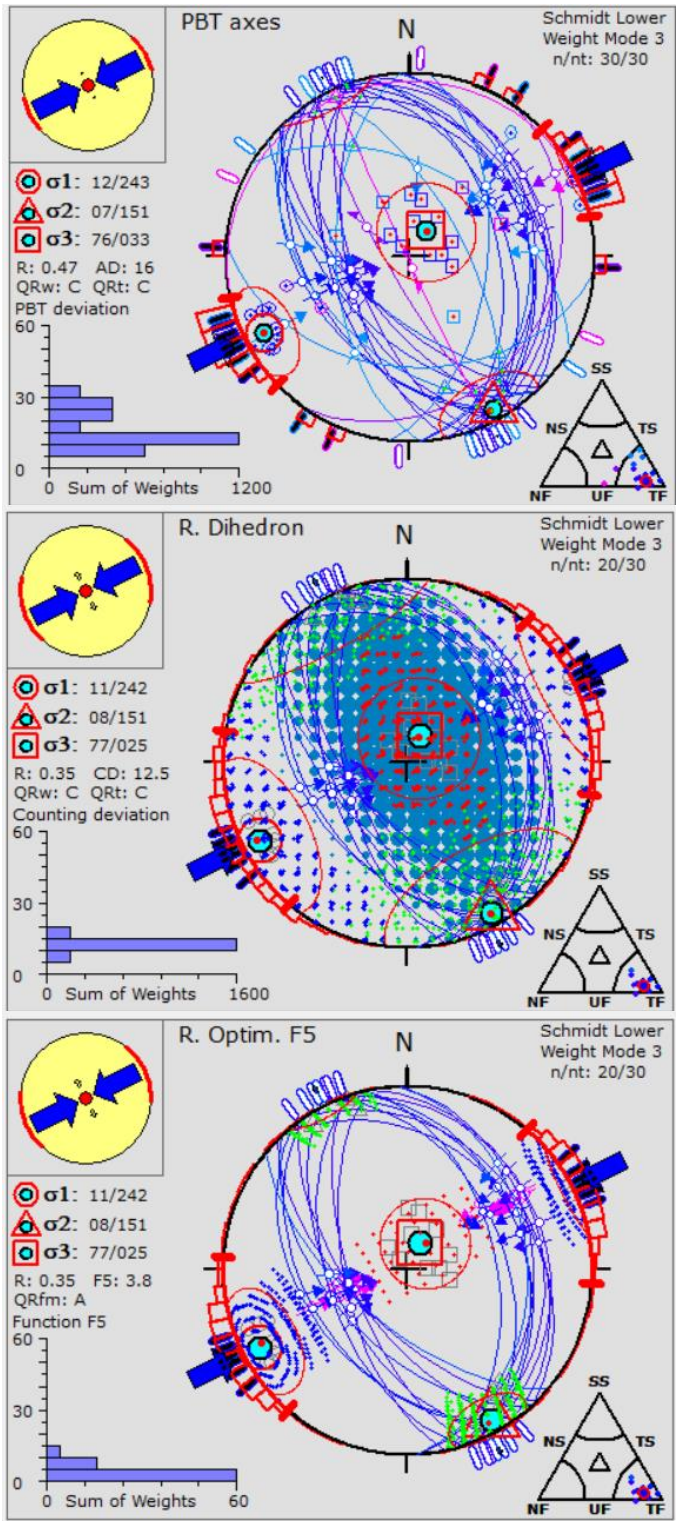

Figure 9: Formal stress inversion of focal mechanism solutions for earthquakes of the 2018 Mandali-Sumar earthquake sequence (see Table 4). The upper panel is the stereographic projection of the focal mechanism solutions using the P, B, and T stress axes. The middle panel shows the results of applying the New Right Dihedron method. The lower panel shows the results of applying the Rotational Optimization method.

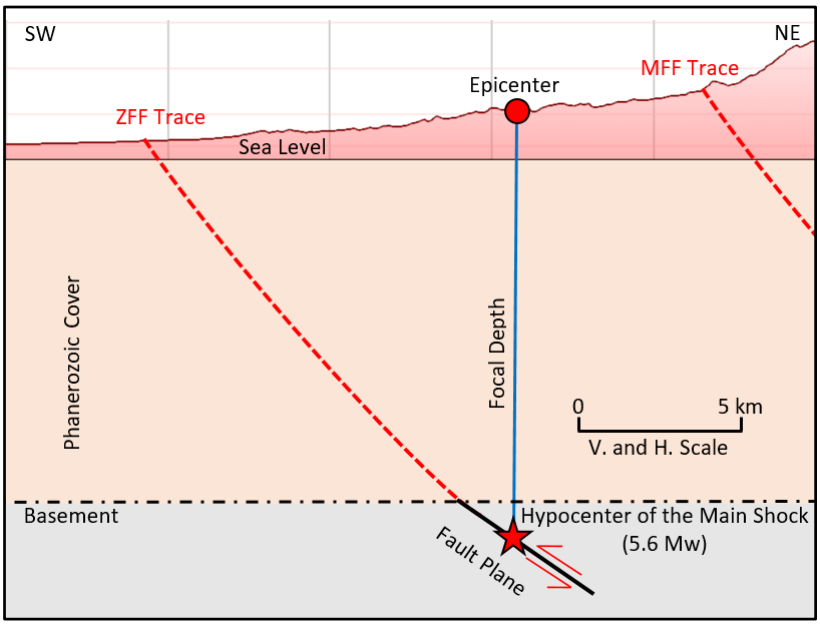

Figure 10: A schematic cross-section through the southwestern limb of the Kuh Gachha-ye Buli anticline where the MFF, ZFF, and earthquake activity exist (see Figure 7). The seismic activity of the 2018 Mandali-Sumar earthquake sequence is related to the displacement of the ZFF within the uppermost basement and the lowermost Phanerozoic cover.

5. CONCLUSIONS

One requirement for locating earthquakes in the Iraq-Iran region is that the area of interest must be surrounded by stations consistently to obtain good azimuthal coverage. Therefore, without using data from stations in both countries to locate earthquakes, this demand cannot be fully satisfied in the Iraq-Iran region. The azimuthal gap, which is one of the most important factors in the estimation of location accuracy, will be reduced by using data from stations in both countries.

After the relocation of the chosen events, it became certain that the epicenters of the 2018 Mandali-Sumar earthquake sequence are located in the Low Folded Zone (Simply Folded Belt) between the Zagros Foredeep Fault in the southwest and the Mountain Front Fault in the northeast. The epicenters in this study have a longitudinal feature with an NW-SE direction, which is the direction of faults in the Zagros Fold-Thrust Belt.

The focal mechanism solutions indicate that the fault has an oblique thrust motion that occurred due to the collision between the Arabian and Iranian plates. The anticlockwise rotational movement of the Arabian plate may be responsible for the oblique motion of the fault surface.

Despite the ambiguity of the two plane solutions being hard to solve, we suggest that the fault is dipping toward the NE because this is the dip direction of the major faults in the area. We believe that the Zagros Foredeep Fault is responsible for the 2018 Mandali-Sumar earthquake sequence. The displacement on the fault surface within the uppermost basement and the lowermost Phanerozoic cover caused the earthquake sequence.

STATEMENTS AND DECLARATIONS

Funding

The research leading to these results received funding from the Lawrence Livermore National Laboratory (LLNL) (Grant numbers B645077 and B650703). Partial financial support was received from the University of Basrah.

Competing Interests

The authors have no relevant financial or non-financial interests to disclose.

ACKNOWLEDGMENT

We would like to extend our gratitude to Robert Herrmann for the CPS software package, Delvaux and Sperner for the TENSOR program, and Wessel and Smith for the GMT software. We owe a debt of gratitude to the MPSN, IRSC, INSN, and GCMT for making the seismic data, catalog, and moment tensor solutions available to us. We are grateful to Dr. Hanan Mahdi and Dr. Haydar Al-Shukri for reviewing the manuscript.

Author Contributions

All authors contributed to the study's conception and design. Material preparation, data collection, and analysis were performed by Wathiq Abdulnaby, Muntadher Al-Kaabi, and Dania Hantoosh. The first draft of the manuscript was written by Wathiq Abdulnaby and all authors commented on previous versions of the manuscript. All authors read and approved the final manuscript.

REFERENCES

Abdulnaby, W. (2019). Structural geology and neotectonics of Iraq, Northwest Zagros. In *Developments in structural geology and tectonics* (Vol. 3, pp. 53–73). Elsevier.

Abdulnaby, W., Mahdi, H., Al-Shukri, H., & Numan, N. M. S. (2014). Stress patterns in Northern Iraq and surrounding regions from formal stress inversion of earthquake focal mechanism solutions. *Pure and Applied Geophysics*, *171*, 2137–2153. https://doi.org/10.1007/s00024-014-0823-x

Al-Kaabi, M., & Abdulnaby, W. (2022). Seismotectonics of the Zagros foredeep fault (ZFF), NE Arabian plate. *Arabian Journal of Geosciences*, *15(1211)*, 1–15. https://doi.org/10.1007/s12517-022-10448-0

Ameen, M. S. (1991a). Alpine geowarpings in the Zagros-Taurus range: Influence on hydrocarbon generation, migration and accumulation. *Journal of Petroleum Geology*, *14*(4), 417–428.

Ameen, M. S. (1991b). Possible forced folding in the Taurus–Zagros belt of northern Iraq. *Geological Magazine*, *128*(6), 561–584.

Ameen, M. S. (1992). Effect of basement tectonics on hydrocarbon generation, migration, and accumulation in northern Iraq (1). *AAPG Bulletin*, *76*(3), 356–370.

Barnhart, W. D., Brengman, C. M. J., Li, S., & Peterson, K. E. (2018). Ramp-flat basement structures of the Zagros Mountains inferred from co-seismic slip and afterslip of the 2017 Mw7. 3 Darbandikhan, Iran/Iraq earthquake. *Earth and Planetary Science Letters*, *496*, 96–107.

Berberian, M. (1995). Master "blind" thrust faults hidden under the Zagros folds: active basement tectonics and surface morphotectonics. *Tectonophysics*, *241*(3–4), 193–224.

Blanc, E.-P., Allen, M. B., Inger, S., & Hassani, H. (2003). Structural styles in the Zagros simple folded zone, Iran. *Journal of the Geological Society*, *160*(3), 401–412. https://doi.org/https://doi.org/10.1144/0016-764902-110

Casciello, E., Vergés, J., Saura, E., Casini, G., Fernandez, N., Blanc, E., Homke, s, & Hunt, D. (2009). Fold patterns and multilayer rheology of the Lurestan Province, Zagros Simply Folded Belt (Iran). *Journal of the Geological Society*, *166*, 947–959. https://doi.org/10.1144/0016-76492008-138

Delvaux, D. (1993). The TENSOR program for paleostress reconstruction: examples from the east African and the Baikal rift zones. *TERRA Nova*, *5*(1), 216.

Delvaux, D., & Sperner, B. (2003). Stress tensor inversion from fault kinematic indicators and focal mechanism data: the TENSOR program. *New Insights into Structural Interpretation and Modelling*, *212*, 75–100.

Emami, H., Vergés, J., Nalpas, T., Gillespie, P., Sharp, I., Karpuz, R., Blanc, E. P., & Goodarzi, M. G. H. (2010). Structure of the Mountain Front Flexure along the Anaran anticline in the Pusht-e Kuh Arc (NW Zagros,

Iran): insights from sand box models. *Geological Society, London, Special Publications*, *330*(1), 155–178. https://doi.org/http://dx.doi.org/10.1144/SP330.9

Farzipour Saein, A., Yassaghi, A., Sherkati, S., & Koyi, H. (2009). Mechanical stratigraphy and folding style of the Lurestan region in the Zagros Fold–Thrust Belt, Iran. *Journal of the Geological Society*, *166*(6), 1101–1115. https://doi.org/10.1144/0016-76492008-162

Fouad, S. F. (2012). *Tectonic Map of Iraq, scale 1:1000000, 3rd ed. GEOSURV, Baghdad, Iraq*.

Fouad, S. F. A. (2012). Western Zagros fold–thrust belt, part I: The low folded zone. *Iraqi Bulletin of Geology and Mining*, *5*, 39–62.

Fouad, S. F. A. (2015). Tectonic map of Iraq, scale 1: 1000 000, 2012. *Iraqi Bulletin of Geology and Mining*, *11*(1), 1–7.

Geiger, L. (1910). Herdbestimmung bei Erdbeben aus den Ankunftszeiten. *Nachrichten von Der Gesellschaft Der Wissenschaften Zu Göttingen, Mathematisch-Physikalische Klasse*, *1910*, 331–349.

Hancock, P. L., & Atiya, M. S. (1979). Tectonic significance of mesofracture systems associated with the Lebanese segment of the Dead Sea transform fault. *Journal of Structural Geology*, *1*(2), 143–153.

Havskov, J., & Ottemoller, L. (2010). *Routine data processing in earthquake seismology*. Springer Science & Business Media.

Herrmann, R. B. (2013). Computer programs in seismology: An evolving tool for instruction and research. *Seismological Research Letters*, *84*(6), 1081–1088.

Jassim, S. Z., & Goff, J. C. (2006). Geology of Iraq. Dolin, prague and moravian museum. *Brno (Czech Republic)*, 341.

Karasözen, E., Nissen, E., Bergman, E. A., & Ghods, A. (2019). Seismotectonics of the Zagros (Iran) from orogen-wide, calibrated earthquake relocations. *Journal of Geophysical Research: Solid Earth*, *124*(8), 9109–9129. https://doi.org/https://doi.org/10.1029/2019JB017336

Lund, B., & Townend, J. (2007). Calculating horizontal stress orientations with full or partial knowledge of the tectonic stress tensor. *Geophysical Journal International*, *170*(3), 1328–1335. https://doi.org/https://doi.org/10.1111/j.1365-246X.2007.03468.x

McQuarrie, N. (2004). Crustal scale geometry of the Zagros fold–thrust belt, Iran. *Journal of Structural Geology*, *26*(3), 519–535.

Mohammed, H. J., & Al-Rahim, A. M. (2020). Seismotectonics and Seismic Source Parameters of the Mid-Eastern Iraq-Western Iran Using Moment Tensor Inversion Technique. *Iraqi Journal of Science*, *61*(7), 1691–1704. https://doi.org/https://doi.org/10.24996/ijs.2020.61.7.18

Nissen, E., Ghods, A., Karasözen, E., Elliott, J. R., Barnhart, W. D., Bergman, E. A., Hayes, G. P., Jamal-Reyhani, M., Nemati, M., & Tan, F. (2019). The 12 November 2017 M w 7.3 Ezgeleh-Sarpolzahab (Iran) earthquake and active tectonics of the Lurestan Arc. *Journal of Geophysical Research: Solid Earth*, *124*(2), 2124–2152. https://doi.org/https://doi.org/10.1029/2018JB016221

Nissen, E., Tatar, M., Jackson, J. A., & Allen, M. B. (2011). New views on earthquake faulting in the Zagros fold-and-thrust belt of Iran. *Geophysical Journal International*, *186*(3), 928–944. https://doi.org/https://doi.org/10.1111/j.1365-246X.2011.05119.x

Numan, N., & Azzawi, N. (1993). Structural and geotectonic interpretation of vergence directions of anticlines in the foreland folds of Iraq. *Abhath Al-Yarmouk, (Pure Science and Engineering)*, *2*, 57–73.

Numan, N. M. S. (1984). Basement control of stratigraphy sequences and structural pattern in Iraq. *Jour. Geol. Soci. Iraq*, *16*(17), 8–24.

Numan, N. M. S. (1997). A plate tectonic scenario for the Phanerozoic succession in Iraq. *Iraqi Geological Journal*, *30*(2), 85–119.

Numan, N. M. S. (2000). Major Cretaceous tectonic events in Iraq. *Rafidain Journal of Science*, *11*(3), 32–52.

Sissakian, V., Shihab, A. T., Al-Ansari, N., & Knutsson, S. (2017). New tectonic finding and its implications on locating Oilfields in parts of the Gulf region. *Journal of Earth Sciences and Geotechnical Engineering*, *7*(3), 51–75.

Tchalenko, J. S., & Braud, J. (1974). Seismicity and structure of the Zagros (Iran): the Main Recent Fault between 33 and 35 N. *Philosophical Transactions of the Royal Society of London. Series A: Mathematical , Physical and Engineering Sciences*, *277*(1262), 1–25. https://doi.org/http://dx.doi.org/10.1098/rsta.1974.0044

Tiira, T., Uski, M., Kortström, J., Kaisko, O., & Korja, A. (2016). Local seismic network for monitoring of a potential nuclear power plant area. *Journal of Seismology*, *20*, 397–417. https://doi.org/https://doi.org/10.1007/s10950-015-9534-8